Nanoscale Research Letters

NANO EXPRESS Open Access

High-Performance Cathode Material of $FeF_3 \cdot 0.33H_2O$ Modified with Carbon Nanotubes and Graphene for Lithium-Ion Batteries

Lu Lu, Sheng Li, Jun Li*, Lifang Lan, Yan Lu, Shuaijun Xu, Si Huang, Chunyang Pan and Fenghua Zhao

Abstract

The $FeF_3 \cdot 0.33H_2O$ cathode material can exhibit a high capacity and high energy density through transfer of multiple electrons in the conversion reaction and has attracted great attention from researchers. However, the low conductivity of $FeF_3 \cdot 0.33H_2O$ greatly restricts its application. Generally, carbon nanotubes (CNTs) and graphene can be used as conductive networks to improve the conductivities of active materials. In this work, the $FeF_3 \cdot 0.33H_2O$ cathode material was synthesized via a liquid-phase method, and the $FeF_3 \cdot 0.33H_2O$/CNT + graphene nanocomposite was successfully fabricated by introduction of CNTs and graphene conductive networks. The electrochemical results illustrate that $FeF_3 \cdot 0.33H_2O$/CNT + graphene nanocomposite delivers a high discharge capacity of 234.2 mAh g^{-1} in the voltage range of 1.8–4.5 V (vs. Li^+/Li) at 0.1 C rate, exhibits a prominent cycling performance (193.1 mAh g^{-1} after 50 cycles at 0.2 C rate), and rate capability (140.4 mAh g^{-1} at 5 C rate). Therefore, the electronic conductivity and electrochemical performance of the $FeF_3 \cdot 0.33H_2O$ cathode material modified with CNTs and graphene composite conductive network can be effectively improved.

Keywords: $FeF_3 \cdot 0.33H_2O$ cathode material, Conductive network, Electrochemical performance, Lithium-ion batteries

Introduction

Rechargeable lithium-ion batteries (LIBs) are the most effective power storage systems for portable electronic devices and considered as promising candidates for electric vehicles (EVs) and hybrid electric vehicles (HEVs) [1]. Compared with traditional fossil energy, LIBs are renewable and clean energy and friendly to the environment. Recently, with the rapid development of LIBs technology, demands for both energy and power density have continuously increased. One key challenge is developing high-performance electrode active materials, and the cathode material is a vital factor for improving the electrochemical properties of LIBs, including the specific capacity, cycling capability, rate capability, etc. [2, 3]. Commercialized cathode materials, such as $LiCoO_2$ [4], $LiMn_2O_4$ [5], and $LiFePO_4$ [6], suffer from low theoretical capacities due to the intercalation reaction involving only a single electron reaction, which cannot satisfy the demands of EVs. In the past several years, multi-electron materials have attracted substantial interest because they can realize the transfer of more than one electron through the conversion reaction [7]. Metal fluorides are ideal cathode materials with high theoretical capacities, energy densities, and operating voltages. Among them, FeF_3 has been regarded as the most suitable cathode material due to its high theoretical specific capacity of 712 mAh g^{-1} ($3e^-$ transfer) and 237 mAh g^{-1} ($1e^-$ transfer), high discharge voltage plateau at approximately 2.7 V, and superb thermal stability [8–10].

Despite these remarkable merits, FeF_3 as a cathode material still has several shortcomings, which have restricted its practical application. The main drawback of FeF_3 is its electronic insulating behavior caused by a high ionicity, which induces a large band gap of the Fe-F bond and eventually leads to a low actual specific capacity, an inferior rate capability, and poor energy

* Correspondence: qhxylijun@gdut.edu.cn
School of Chemical Engineering and Light Industry, Guangdong University of Technology, No. 100 Waihuan xi Road, Guangzhou Higher Education Mega Center, Panyu District, Guangzhou 510006, China

efficiency [11–13]. In order to resolve these issues, various strategies have been adopted to overcome the poor electronic and ionic conductivities. Generally, the methods to improve conductivity can be summarized in three aspects as follows: (1) element doping. Element doping can effectively decrease the band gap and actively effect microcrystal growth [14, 15]. Rahman et al. prepared Co-doped iron fluoride ($Fe_{0.9}Co_{0.1}F_3{\cdot}0.5H_2O$) by a non-aqueous precipitation method, resulting in a high discharge capacity of 227 mAh g^{-1} at 0.1 C between 1.8 and 4.5 V [14]. (2) Surface coating. Modification by introducing a coating layer can significantly shorten the Li^+ transport length and alleviate volume changes [16]. Ma et al. successfully fabricated FeF_3 coated with poly (3,4-ethylenedioxythiophene) (PEDOT) via a novel in situ polymerization method, and the sample exhibited a high power capability of 120 mAh g^{-1} at 1 A g^{-1} at room temperature due to the improved ionic and electronic transport in the electrode [17]. (3) Fabricating composite with conductive additives. It can substantially enhance the cycling and rate performance of the FeF_3 cathode material [18–21]. Jung et al. obtained FeF_3/ordered mesoporous carbon (OMC) nanocomposite that showed a high reversible specific capacity (178 mAh g^{-1} at 0.1 C during the second cycle in the voltage range of 2.0–4.5 V) and better cycling stabilities (capacity fading of 8.8%) than bulk FeF_3 (capacity fading of approximately 42%) at 30 cycles [22]. Noticeably, the fabrication of composite with conductive network is the most beneficial approach to improve both the ionic and electronic conductivities to eventually enhance the electrochemical performance of the cathode material.

Iron(III) fluoride cathode materials with different amounts of hydration water, for example, $FeF_3{\cdot}0.33H_2O$ [23], $FeF_3{\cdot}0.5H_2O$ [24], $FeF_3{\cdot}3H_2O$ [25], and FeF_3 [26], have been extensively reported. Among them, hexagonal tungsten bronze-type $FeF_3{\cdot}0.33H_2O$ demonstrated that with the best electrochemical property, its characteristic one-dimensional hexagonal cavity is convenient for efficient Li^+ transport and can facilitate electrolyte penetration [27]. In addition, the unique structure can effectively limit the movement of water and stabilize the crystal structure. Different functionalized carbon matrixes have been used as conductive networks, but overall, carbon nanotubes (CNTs) and graphene exhibit significant potential as conductive medium due to their distinguished electronic conductivities and excellent stabilities [28–31]. Graphene, with its large specific area, can promote sufficient contact at the electrode and electrolyte interface, and the graphene network plays an important role in electron transfer and ion migration. Furthermore, graphene provides excellent mechanical stability, which contributes to the bend and stretch of electrode [32, 33].

In this study, nanostructured $FeF_3{\cdot}0.33H_2O$ cathode material was synthesized via a liquid-phase method, and then, the precursor was milled with CNTs followed by sintering to obtain $FeF_3{\cdot}0.33H_2O$/CNT composite that was further mixed with graphene conducting paste without a binder. Finally, the CNTs and graphene co-modified $FeF_3{\cdot}0.33H_2O$ nanocomposite was successfully prepared. The CNTs with intrinsic flexibility and large specific surface area can greatly facilitate the electron transport, and graphene with high mechanical strength and high chemical stability can effectively buffer the volume change and provides a support for electrochemical reaction [31, 34, 35]. Moreover, the interconnecting of CNTs and graphene sheets can construct an integrated three-dimensional conductive framework, which tremendously promotes Li^+ diffusion and simultaneously increases the structure stability. Therefore, compared to the $FeF_3{\cdot}0.33H_2O$ composite with a single conductive network of CNTs and pure $FeF_3{\cdot}0.33H_2O$, $FeF_3{\cdot}0.33H_2O$ nanocomposite with CNTs and graphene networks exhibits superior electrochemical properties. The morphologies, crystal structures, and electrochemical performances of all the samples were systematically investigated.

Results and Discussion

Structural and Morphology Analysis

Thermogravimetric-differential scanning calorimetry (TG-DSC) measurement was carried out to confirm the dehydration temperature of the $FeF_3{\cdot}3H_2O$ precursor and the result is shown in Fig. 1a. Four stages of the weight loss curve are found in the regions of 30–110 °C, 110–250 °C, 250–450 °C, and 450–700 °C. In the first stage of 30–110 °C, a slight weight loss of approximately 3% can be attributed to phase transformation of crystal. In the second stage of 110–250 °C, the TG curve has a rapid weight loss of about 15% and the DSC curve shows an evident endothermic peak around 170 °C; the corresponding reaction process is the removal of hydration water (2.67 H_2O) from $FeF_3{\cdot}3H_2O$. In the third stage of 250–450 °C, the weight loss is about 6% which may be due to the removal of hydration water for $FeF_3{\cdot}0.33H_2O$ transforming to FeF_3 and a weak exothermic peak is observed from the DSC curve. In the last stage of 450–700 °C, a little weight loss of about 4% is probably due to the decomposition of FeF_3. According to these results, the precursor was dried at 80 °C in a vacuum oven to remove the absorbed water and calcinated at 240 °C to obtain $FeF_3{\cdot}0.33H_2O$.

X-ray diffraction (XRD) measurements were conducted to investigate the crystal structure of the synthesized samples. The XRD patterns of $FeF_3{\cdot}0.33H_2O$, $FeF_3{\cdot}0.33H_2O$/CNT, and $FeF_3{\cdot}0.33H_2O$/C + G are depicted in Fig. 1b. All samples reveal diffraction peaks positioned

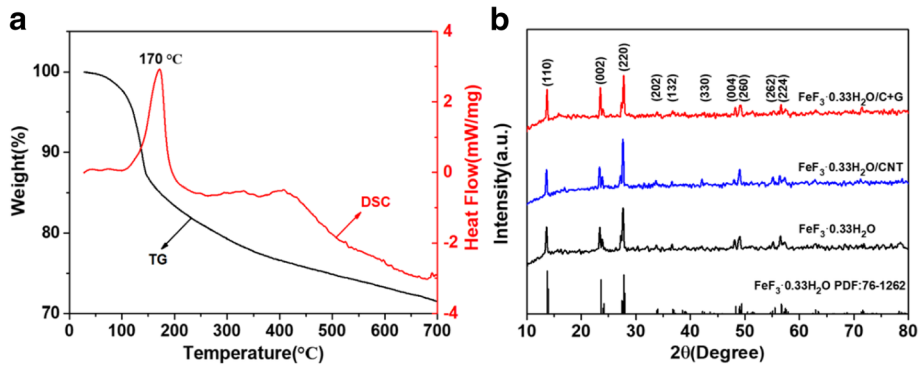

Fig. 1 **a** TG-DSC curve of the $FeF_3{\cdot}3H_2O$ precursor measured from 30 to 700 °C at a heating rate of 10 °C min^{-1} under an argon atmosphere. **b** XRD patterns of $FeF_3{\cdot}0.33H_2O$, $FeF_3{\cdot}0.33H_2O$/CNT, and $FeF_3{\cdot}0.33H_2O$/C + G

at 2θ = 13.79°, 23.62°, and 27.80° in accordance with the (110), (002), and (220) facets, which matched well with the standard spectrum of hexagonal tungsten bronze structure $FeF_3{\cdot}0.33H_2O$ (PDF No. 76-1262) [36]. No evident characteristic peak of CNTs and graphene are observed in the XRD pattern of the $FeF_3{\cdot}0.33H_2O$/CNT and $FeF_3{\cdot}0.33H_2O$/C + G samples, which is mainly due to the low contents of CNTs and graphene.

The SEM and EDS measurements were performed to analyze the microstructure of the composites. The morphologies and particle sizes of $FeF_3{\cdot}0.33H_2O$, $FeF_3{\cdot}0.33H_2O$/CNT and $FeF_3{\cdot}0.33H_2O$/C + G nanocomposites are shown in Fig. 2. As distinctly seen from Fig. 2a, the particle size of pure $FeF_3{\cdot}0.33H_2O$ is around 100 nm, and the particles are uniform in size and well distributed, slight aggregation is observed, and the particle size of $FeF_3{\cdot}0.33H_2O$ can be further confirmed by particle size distribution diagram shown in Fig. 2e. Figure 2b presents the morphology of $FeF_3{\cdot}0.33H_2O$/CNT nanocomposite. Clearly, the conductive network of CNTs is intimately intertwined on the surface of the $FeF_3{\cdot}0.33H_2O$ particles. For the $FeF_3{\cdot}0.33H_2O$/C + G nanocomposite, the surface of the $FeF_3{\cdot}0.33H_2O$ particles is wrapped by CNTs and graphene sheets; as shown in Fig. 2c, the $FeF_3{\cdot}0.33H_2O$ particles and CNTs are well covered by graphene sheets. In addition, the graphene sheets are preserved well-layered structure in the $FeF_3{\cdot}0.33H_2O$/C + G nanocomposite, which can provide a fast channel for Li^+ transport. The conductive contact between the $FeF_3{\cdot}0.33H_2O$ material and current collector can be significantly improved by CNTs and graphene due to their outstanding electronic conductivity. Especially graphene with a large surface area can provide an additional transport channel for Li-ion diffusion, which makes the $FeF_3{\cdot}0.33H_2O$/C + G nanocomposite with superior electrochemical performance. EDS test was carried out to further investigate the elemental composition of the $FeF_3{\cdot}0.33H_2O$/C + G nanocomposite. The elements of Fe, F, O, and C can be observed from the EDS image in Fig. 2d.

The morphology and detailed microstructure of the $FeF_3{\cdot}0.33H_2O$/C + G nanocomposite were further studied by TEM, and the TEM images are displayed in Fig. 3. As shown in Fig. 3a, b, the $FeF_3{\cdot}0.33H_2O$ particles and CNTs and graphene sheets are closely interconnected with each other, which is consistent with the result of the SEM images. The HRTEM image shown in Fig. 3c offers no evident delineation between the bulk and wrapping layer; the lattice fringe spacing of 0.64 nm coincides with the (110) facet of $FeF_3{\cdot}0.33H_2O$. The SAED pattern of the $FeF_3{\cdot}0.33H_2O$/C + G nanoparticle is shown in Fig. 3d; the planes of (110), (002), (220), (132), and (004) correspond to the XRD results, which indexed to the hexagonal tungsten bronze structure $FeF_3{\cdot}0.33H_2O$. The $FeF_3{\cdot}0.33H_2O$/C + G nanocomposite with small particle size and superb conductive network structure, favors sufficient contact between the electrode material and electrolyte and facilitates Li-ion transport; therefore, better electrochemical performance can be achieved.

Electrochemical Characterization

To investigate the electrochemical properties of all samples, galvanostatic charge/discharge tests were implemented in the voltage range of 1.8–4.5 V (vs. Li^+/Li), and this voltage range allows only one electron reaction to occur. The charge-discharge profiles of all samples are shown in Fig. 4. The initial charge-discharge curves of the three electrodes at 0.1 C (1 C = 237 mAh g^{-1}) rate are shown in Fig. 4a; the pristine $FeF_3{\cdot}0.33H_2O$ electrode exhibits the lowest initial discharge capacity of 217.5 mAh g^{-1}, which may be due to the poor electronic conductivity of $FeF_3{\cdot}0.33H_2O$. While the $FeF_3{\cdot}0.33H_2O$/CNT and $FeF_3{\cdot}0.33H_2O$/C + G electrodes deliver higher initial discharge capacities of approximately

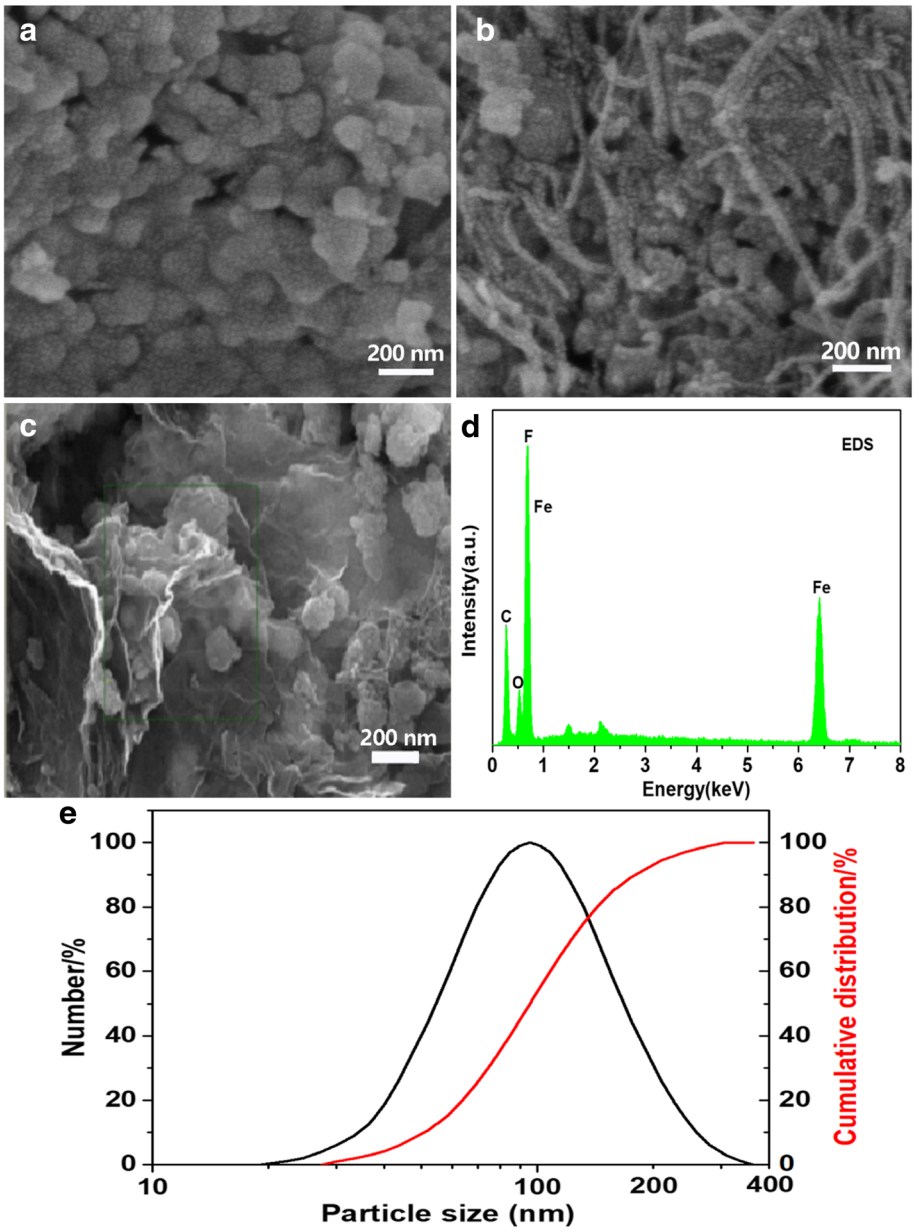

Fig. 2 SEM images, **a** $FeF_3{\cdot}0.33H_2O$, **b** $FeF_3{\cdot}0.33H_2O$/CNT, and **c** $FeF_3{\cdot}0.33H_2O$/C + G. **d** EDS of the $FeF_3{\cdot}0.33H_2O$/C + G. **e** Particle size distribution diagram of $FeF_3{\cdot}0.33H_2O$

225.1 mAh g^{-1} and 234.2 mAh g^{-1}, respectively. In our test, the initial discharge capacity of the $FeF_3{\cdot}0.33H_2O$/C + G electrode is only 16.7 mAh g^{-1} higher than that of the pristine $FeF_3{\cdot}0.33H_2O$ electrode, illustrating CNTs and graphene almost deliver no capacity in the $FeF_3{\cdot}0.33H_2O$/C + G sample. The slightly increased capacity can be attributed to the CNTs and graphene incorporation enhanced the electron transport and reduced electrochemical polarization. From the initial charge-discharge curves of all electrodes, all the curves have an evident discharge plateau at 2.7 V due to the insertion reaction ($Li^+ + e^- + FeF_3 \cdot 0.33H_2O \rightarrow LiFeF_3 \cdot 0.33H_2O$). The charge-discharge profiles of different cycles at 0.2 C rate are presented in Fig. 4b–d. As shown in Fig. 4b, the $FeF_3{\cdot}0.33H_2O$ electrode only delivers a capacity of 146.2 mAh g^{-1} at 0.2 C rate after 50 cycles. The $FeF_3{\cdot}0.33H_2O$/CNT electrode delivers a capacity of 170.3 mAh g^{-1} after 50 cycles shown in Fig. 4c. It is worth noting that the $FeF_3{\cdot}0.33H_2O$/C + G electrode still retain a capacity of 193.1 mAh g^{-1} even after 50 cycles shown in Fig. 4d. In addition, the $FeF_3{\cdot}0.33H_2O$/C + G electrode presents the lowest charge voltage plateau and the highest

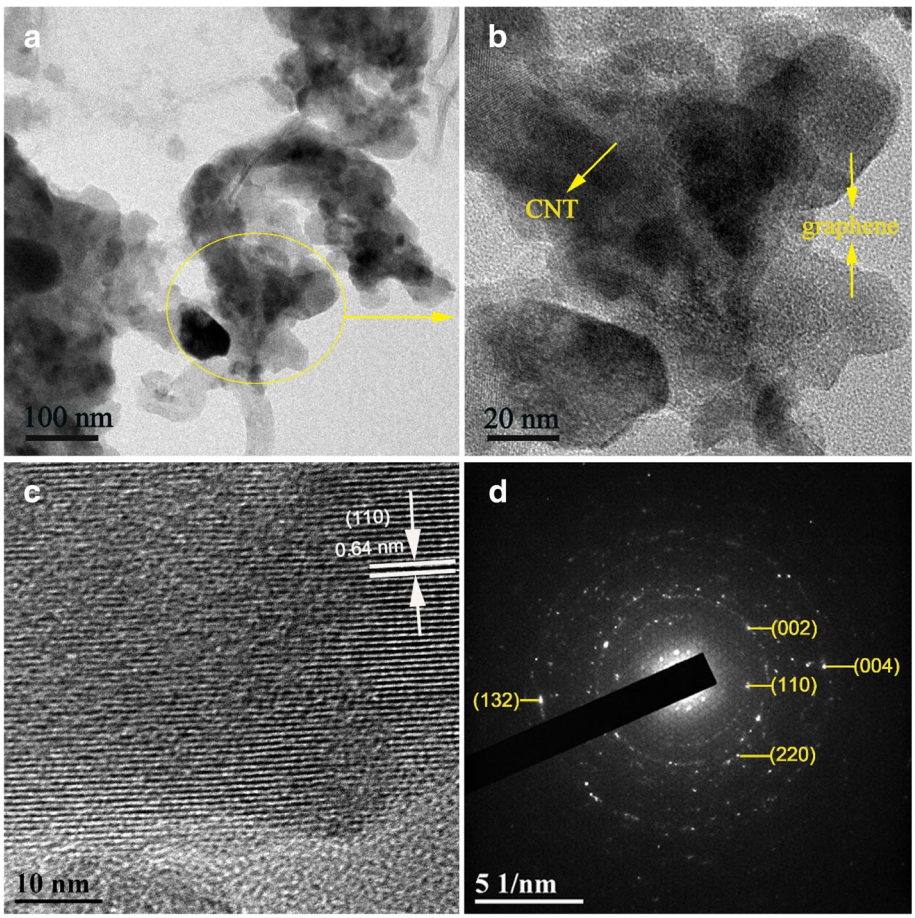

Fig. 3 **a**, **b** TEM images of $FeF_3{\cdot}0.33H_2O$/C + G nanocomposite. **c** HRTEM image of $FeF_3{\cdot}0.33H_2O$/C + G nanocomposite. **d** SAED image of $FeF_3{\cdot}0.33H_2O$/C + G nanocomposite

discharge voltage plateau, demonstrating that it has the smallest electrochemical polarization and excellent reversibility, thus mitigate the voltage hysteresis. The better performance of $FeF_3{\cdot}0.33H_2O$/CNT and $FeF_3{\cdot}0.33H_2O$/C + G electrodes demonstrate that adding CNTs and graphene can effectively improve the conductivity of the $FeF_3{\cdot}0.33H_2O$ cathode material. Particularly, the $FeF_3{\cdot}0.33H_2O$/C + G electrode exhibits the best electrochemical performance due to the interlacing of CNTs and graphene forms a three-dimensional conductive structure, which tremendously facilitate the transport of Li-ion, and thus resulting in promoting the intercalation process of Li-ions [37, 38].

To further demonstrate the excellent cycling stability of the $FeF_3{\cdot}0.33H_2O$/C + G nanocomposite, the cycling capabilities of the $FeF_3{\cdot}0.33H_2O$, $FeF_3{\cdot}0.33H_2O$/CNT, and $FeF_3{\cdot}0.33H_2O$/C + G electrodes up to the 50th cycle at 0.2 C rate in the voltage range of 1.8–4.5 V (vs. Li^+/Li) are shown in Fig. 5a. The $FeF_3{\cdot}0.33H_2O$ electrode with a rapid capacity decay and a poor capacity retention of approximately 70.83% (capacity fading rate of 0.58% per cycle) after 50 cycles. The $FeF_3{\cdot}0.33H_2O$/CNT electrode shows a capacity retention of about 79.65% (0.41% fading per cycle) after 50 cycles. Notably, the $FeF_3{\cdot}0.33H_2O$/C + G electrode achieve the highest capacity retention of 85.48% (only 0.29% fading per cycle) after 50 cycles. Moreover, the coulombic efficiency of the $FeF_3{\cdot}0.33H_2O$/C + G electrode can reach up to over 99% during the Li^+ insertion and extraction processes. The above results demonstrate that CNTs and graphene can improve the electronic conductivity and enhance the discharge capacities of $FeF_3{\cdot}0.33H_2O$. Particularly, the $FeF_3{\cdot}0.33H_2O$/C + G electrode exhibits the best cycling performance, illustrating higher electrical conductivity, better reversibility, and lower polarization after adding of CNTs and graphene. CNTs with high surface area supply sufficient pathway for electron transfer and the graphene works as an excellent conductive network for enabling fast Li^+ transport between the electrolyte and electrode [28, 35]. Moreover, the $FeF_3{\cdot}0.33H_2O$ particles and CNTs can work as spacers to impede the stacking of graphene sheets and

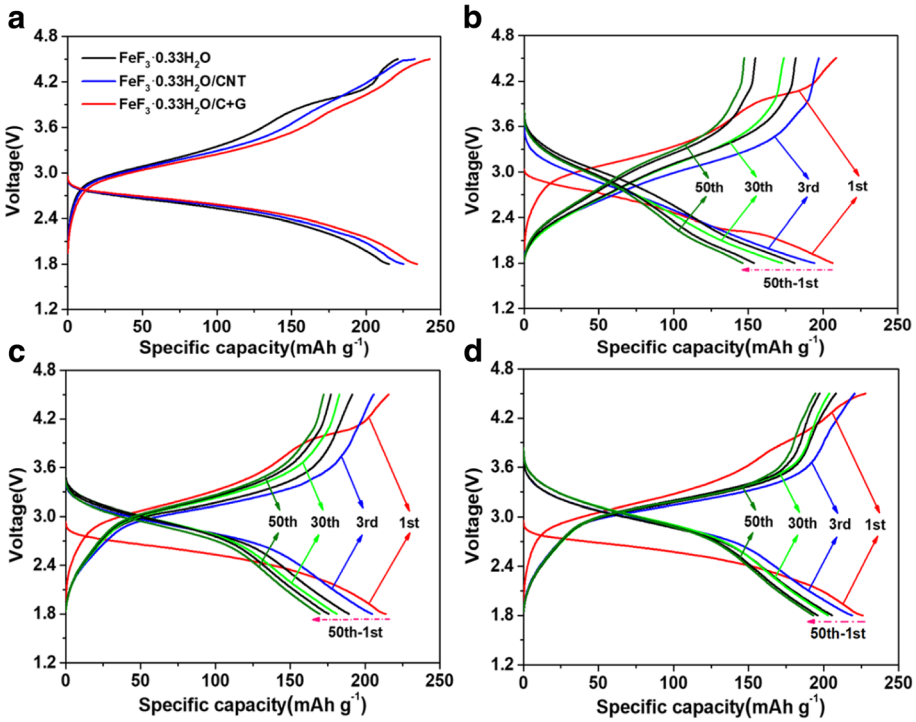

Fig. 4 **a** The initial charge-discharge profiles of $FeF_3{\cdot}0.33H_2O$, $FeF_3{\cdot}0.33H_2O$/CNT, and $FeF_3{\cdot}0.33H_2O$/C + G electrodes at 0.1 C rate. Charge and discharge profiles of different cycles (1st, 3rd, 30th, 50th) at 0.2 C rate, **b** $FeF_3{\cdot}0.33H_2O$, **c** $FeF_3{\cdot}0.33H_2O$/CNT, and **d** $FeF_3{\cdot}0.33H_2O$/C + G

thus provide high active surface area. Therefore, the interaction of $FeF_3{\cdot}0.33H_2O$ particles and CNTs and graphene can significantly improve the cycling performance.

The rate capabilities of the $FeF_3{\cdot}0.33H_2O$, $FeF_3{\cdot}0.33H_2O$/CNT, and $FeF_3{\cdot}0.33H_2O$/C + G electrodes were evaluated at 0.1 C, 0.5 C,1 C, 3 C, and 5 C rates and then again at 0.1 C rate and results are displayed in Fig. 5b. The discharge capacities of all samples are decreased with increased current density. As expected, the $FeF_3{\cdot}0.33H_2O$/C + G electrode presents a superior rate performance among the three electrodes and delivers average discharge capacities of 228 mAh g^{-1}, 210.7 mAh g^{-1}, 194.4 mAh g^{-1}, 170.5 mAh g^{-1}, and 140.4 mAh g^{-1} at 0.1 C, 0.5 C, 1 C, 3 C, and 5 C rates. When the rate is returned to 0.1 C, the electrode can still deliver a discharge capacity of 226.7 mAh g^{-1}. For comparison, $FeF_3{\cdot}0.33H_2O$ and $FeF_3{\cdot}0.33H_2O$/CNT electrodes show inferior rate performance; they deliver poor discharge capacities of 81.7 mAh g^{-1} and 115.7 mAh g^{-1} at 5 C rate, which are remarkably lower than that of $FeF_3{\cdot}0.33H_2O$/C + G electrode. As a result, the rate capability of the $FeF_3{\cdot}0.33H_2O$/C + G electrode is significantly improved compared to those of $FeF_3{\cdot}0.33H_2O$ without or with a single CNT conductive network. Therefore, the good rate capability of the $FeF_3{\cdot}0.33H_2O$/C + G

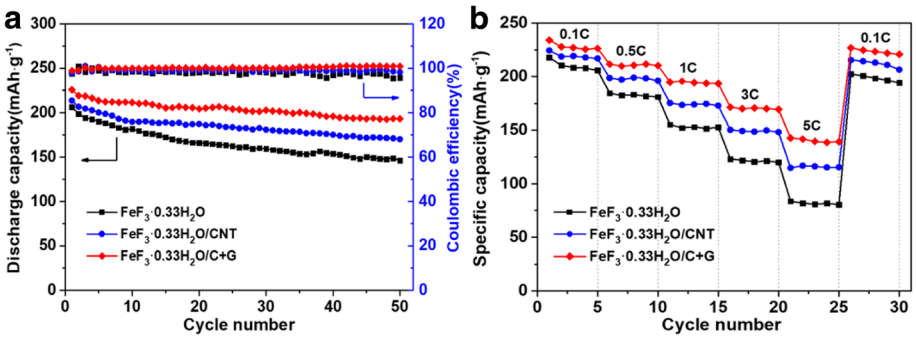

Fig. 5 **a** Cycling performances of $FeF_3{\cdot}0.33H_2O$, $FeF_3{\cdot}0.33H_2O$/CNT, and $FeF_3{\cdot}0.33H_2O$/C + G electrodes at 0.2 C rate. **b** Rate performances of $FeF_3{\cdot}0.33H_2O$, $FeF_3{\cdot}0.33H_2O$/CNT, and $FeF_3{\cdot}0.33H_2O$/C + G electrodes at different current density

electrode result from the CNTs and graphene conductive networks, which enhanced the electronic conductivity, and above all, the constructed three-dimensional conductive network is beneficial for Li-ion insertion and extraction between electrodes.

Cyclic voltammogram (CV) measurements were carried out to further examine the electrochemical properties of the $FeF_3{\cdot}0.33H_2O$, $FeF_3{\cdot}0.33H_2O$/CNT, and $FeF_3{\cdot}0.33H_2O$/C + G electrodes at a scan rate of 1 mV s^{-1} between 1.8 V and 4.5 V (vs. Li^+/Li) which are shown in Fig. 6. The three curves display similar shapes with apparent oxidation/reduction peaks corresponding to delithiation/lithiation processes. The oxidation and reduction peaks of the $FeF_3{\cdot}0.33H_2O$/C + G electrode are detected at 3.32 V and 2.78 V, and the potential interval (ΔE_p) is 0.54 V. While the ΔE_p values of the $FeF_3{\cdot}0.33H_2O$ and $FeF_3{\cdot}0.33H_2O$/CNT electrodes are 0.59 V and 0.62 V, respectively. Smaller ΔE_p value indicates a smaller electrochemical polarization and a better reversibility of the electrode. In addition, the $FeF_3{\cdot}0.33H_2O$/C + G electrode exhibits a higher current and a larger area than those of the $FeF_3{\cdot}0.33H_2O$ and $FeF_3{\cdot}0.33H_2O$/CNT electrodes. The area surrounded by the CV curve represents the capacity of the material; the larger area is related to the higher capacity, and the change rate of area represents the decay rate of capacity. The results reveal that the $FeF_3{\cdot}0.33H_2O$/C + G electrode has a higher capacity and better reversibility, which is well consistent with the galvanostatic charge/discharge tests.

Electrochemical impedance spectroscopy (EIS) measurements were performed to explore the electrochemical reaction kinetics behavior of the $FeF_3{\cdot}0.33H_2O$, $FeF_3{\cdot}0.33H_2O$/CNT, and $FeF_3{\cdot}0.33H_2O$/C + G electrodes after the 3rd cycle and 50th cycle, and results are shown in Fig. 7a, b. All the Nyquist plots of the electrodes after activation are consisted of a semicircle and a sloping line. The semicircle in the high frequency is related to the charge transfer resistance (R_{ct}), which represents the reaction kinetics of the electrode. The smaller radius of semicircle demonstrates the easier transport of Li^+ and the electron transfer between the electrolyte and electrode interface, and the sloping line in the low frequency is associated with the Warburg resistance (Z_w) of Li^+ diffusion in the bulk of cathode material [39]. The corresponding equivalent circuit model was constructed to illustrate the impedance spectra shown in Fig. 7e; the uncompensated ohmic resistance (R_s) represents the resistance of the electrolyte and electrode material, and the constant phase-angle element (CPE) represents the double-layer capacitance and passive film capacitance [40]. The impedance values of R_s and R_{ct} for the three electrodes after the 3rd and 50th cycle are listed in Table 1. No significant difference of R_s values for the three electrodes after the 3rd cycle is noted. However, the R_{ct} value (50.9 Ω) of the $FeF_3{\cdot}0.33H_2O$/C + G electrode is evidently lower than those of the $FeF_3{\cdot}0.33H_2O$ (115.7 Ω) and $FeF_3{\cdot}0.33H_2O$/CNT (68.2 Ω) electrodes, which indicated less polarization of the $FeF_3{\cdot}0.33H_2O$/C + G electrode. Moreover, the R_{ct} value of the $FeF_3{\cdot}0.33H_2O$/C + G electrode is 86.5 Ω after the 50th cycle, which is also the smallest among the three electrodes. The lower R_{ct} value of the electrode after activation suggested better charge transfer kinetics behavior. The lithium ion diffusion coefficients (D_{Li+}) of the $FeF_3{\cdot}0.33H_2O$, $FeF_3{\cdot}0.33H_2O$/CNT, and $FeF_3{\cdot}0.33H_2O$/C + G electrodes are calculated from the following equation [41],

$$D_{Li+} = \frac{R^2T^2}{2A^2n^4F^4C^2\sigma_\omega^2} \quad (1)$$

In Eq. (1), R is the gas constant, T is the absolute temperature, A is the surface area of electrode, n is the number of electrons involved in the redox reaction, F is the Faraday constant, C is the molar concentration of Li^+, and σ_ω is the Warburg coefficient which can be obtained from the following relationship,

$$Z' = R_s + R_{ct} + \sigma_\omega \omega^{-1/2} \quad (2)$$

where Z' is the real part of impedance and ω is the angular frequency in the low-frequency region. The linearity of Z' and $\omega^{-1/2}$ after the 3rd cycle and 50th cycle are shown in Fig. 7c, d. The Li^+ diffusion coefficients of the three electrodes are listed in Table 1. The D_{Li+} value (1.67×10^{-12} cm^2 s^{-1}) of the $FeF_3{\cdot}0.33H_2O$/C + G electrode after the 3rd cycle is higher than those of the $FeF_3{\cdot}0.33H_2O$/CNT (1.19×10^{-12} cm^2 s^{-1}) and $FeF_3{\cdot}0.33H_2O$ (7.63×10^{-13} cm^2 s^{-1}). In addition, the D_{Li+} values of the $FeF_3{\cdot}0.33H_2O$, $FeF_3{\cdot}0.33H_2O$/CNT, and $FeF_3{\cdot}0.33H_2O$/C + G electrodes after the 50th

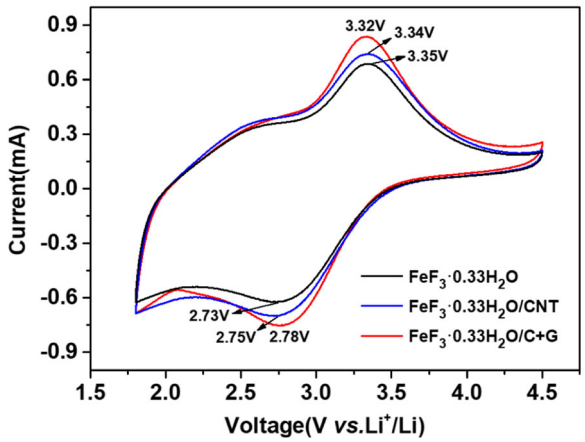

Fig. 6 CV curves of $FeF_3{\cdot}0.33H_2O$, $FeF_3{\cdot}0.33H_2O$/CNT, and $FeF_3{\cdot}0.33H_2O$/C + G electrodes at a scan rate of 1 mV s^{-1}

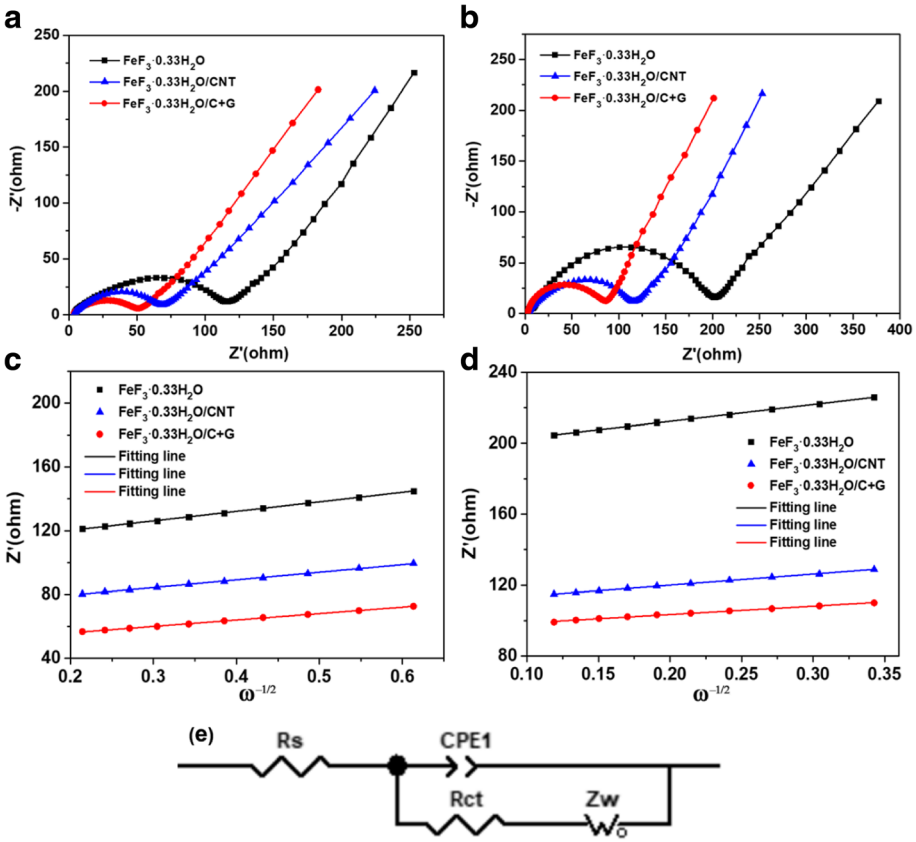

Fig. 7 The Nyquist plots of $FeF_3{\cdot}0.33H_2O$, $FeF_3{\cdot}0.33H_2O$/CNT, and $FeF_3{\cdot}0.33H_2O$/C + G electrodes; **a** the 3rd cycle and **b** the 50th cycle. The relationship plots of $FeF_3{\cdot}0.33H_2O$, $FeF_3{\cdot}0.33H_2O$/CNT, and $FeF_3{\cdot}0.33H_2O$/C + G electrodes between Z' and $\omega^{-1/2}$ at low-frequency region; **c** the 3rd cycle and **d** the 50th cycle. **e** The corresponding equivalent circuit model of EIS

cycle are 2.96×10^{-13} cm^2 s^{-1}, 7.10×10^{-13} cm^2 s^{-1}, and 1.21×10^{-12} cm^2 s^{-1}, respectively. Apparently, the D_{Li+} values of the $FeF_3{\cdot}0.33H_2O$/C + G electrode are the highest among the three electrodes, indicating that the $FeF_3{\cdot}0.33H_2O$/C + G shows better electrode reaction kinetics. The results confirm that the conductive network constructed by CNTs and graphene can effectively reduce the polarization of $FeF_3{\cdot}0.33H_2O$/C + G electrode, which contribute to excellent electrochemical performance.

Conclusions

In summary, the $FeF_3{\cdot}0.33H_2O$ cathode material was successfully synthesized by a liquid-phase method, and the $FeF_3{\cdot}3H_2O$ precursor was milled with CNTs conductive network followed by sintering to obtain $FeF_3{\cdot}0.33H_2O$/CNT nanocomposite, and then mixed with graphene conducting paste without a binder to obtain the $FeF_3{\cdot}0.33H_2O$/C + G nanocomposite. The functional network consisted of CNTs and graphene provides an effective strategy to improve the electronic conductivity of $FeF_3{\cdot}0.33H_2O$ cathode material. The $FeF_3{\cdot}0.33H_2O$/C + G nanocomposite exhibits better electrochemical performances with increased specific capacity, extended cyclic lifespan, and enhanced rate capability than that of pure $FeF_3{\cdot}0.33H_2O$. The EIS results also indicate that the $FeF_3{\cdot}0.33H_2O$/C + G electrode has the best electrochemical reaction kinetics behavior. The outstanding electrochemical performances of $FeF_3{\cdot}0.33H_2O$/C + G

Table 1 R_s, R_{ct}, and D_{Li+} values of $FeF_3{\cdot}0.33H_2O$, $FeF_3{\cdot}0.33H_2O$/CNT, and $FeF_3{\cdot}0.33H_2O$/C + G electrodes after the 3rd and 50th cycle

Samples	3rd cycle			50th cycle		
	R_s (Ω)	R_{ct} (Ω)	D_{Li+} (cm^2 s^{-1})	R_s (Ω)	R_{ct} (Ω)	D_{Li+} (cm^2 s^{-1})
$FeF_3{\cdot}0.33H_2O$	4.2	115.7	7.63×10^{-13}	8.2	202.6	2.96×10^{-13}
$FeF_3{\cdot}0.33H_2O$/CNT	4.0	68.2	1.19×10^{-12}	4.2	115.7	7.10×10^{-13}
$FeF_3{\cdot}0.33H_2O$/C + G	3.8	50.9	1.67×10^{-12}	3.9	86.5	1.21×10^{-12}

Equation 1 calculate the diffusion coefficient of Li^+
Equation 2 a relationship between σ_ω and Z'

can be attributed to the constructed three-dimensional conductive networks by CNTs and graphene, improving the electronic conductivity, facilitating the Li^+ and electron transport, thus enhancing the cycling and rate capabilities. Therefore, the $FeF_3{\cdot}0.33H_2O$ cathode material modified with CNTs and graphene showed excellent electrochemical properties and exhibited great promise as a cathode material for LIBs application.

Methods

Synthesis of $FeF_3{\cdot}0.33H_2O$ Powder

$FeF_3{\cdot}0.33H_2O$ powder was synthesized via a liquid-phase method followed by an annealing treatment. For the synthesis of $FeF_3{\cdot}0.33H_2O$ powder, $Fe(NO_3)_3{\cdot}9H_2O$ (Aladdin, 99.99%) and NH_4F (Aladdin, 98%) were utilized as the iron and fluorine sources, respectively, and polyethylene glycol (PEG400, Aldrich, 20%) was used as a dispersant. First, 3.1 g $Fe(NO_3)_3{\cdot}9H_2O$ was dissolved in 20 mL ethanol in a Teflon-lined stainless-steel autoclave, and then, three drops of PEG400 were added. Next, the solution was ultrasonicated for 10 min to obtain solution A. Then, 0.85 g NH_4F was dissolved in 5 mL of deionized water and ultrasonicated to form solution B. Solution B was added dropwise into the constantly stirred solution A, and the yellow solution gradually became colorless, eventually gained conglobate precipitates. After stewing for 12 h at room temperature, the precipitates were alternately washed with deionized water and ethanol several times and then dried at 80 °C for 12 h in a vacuum oven. After cooling to room temperature naturally, the precipitates were ground into powder to obtain $FeF_3{\cdot}3H_2O$ precursor and then transferred into a tube furnace for calcination at 240 °C for 3 h under an argon atmosphere to remove the crystal water. Finally, the $FeF_3{\cdot}0.33H_2O$ powder was obtained.

Preparation of $FeF_3{\cdot}0.33H_2O$/CNT + Graphene Combination Electrode

To prepare $FeF_3{\cdot}0.33H_2O$ with CNTs and graphene conductive networks, optimized amount of 5 wt% CNTs were added into the as-prepared precursor, uniformly ground and heated at tube furnace (240 °C for 3 h) under an argon atmosphere to obtain $FeF_3{\cdot}0.33H_2O$/CNT powder. Then, 0.5 g $FeF_3{\cdot}0.33H_2O$/CNT powder was added into 1.5 mL graphene *N*-methyl pyrrolidinone paste (Aladdin, graphene content: 1–1 .5wt%), stirred 4 h to form a homogeneous slurry. The slurry was pasted on an Al foil and dried at 85 °C overnight to obtain the $FeF_3{\cdot}0.33H_2O$/CNT + graphene (denoted as $FeF_3{\cdot}0.33H_2O$/C + G) combination electrode. Notably, the process of making combination electrode did not require the addition of a binder.

Characterization

Thermogravimetric-differential scanning calorimetry (TG-DSC) measurement of the precursor was carried out in the temperature range from 30 to 700 °C at a heating rate of 10 °C min^{-1} under an argon atmosphere. The crystal structures of all the samples were characterized by X-ray diffraction (XRD, Bruker AXS D8, Germany) with Cu Kα radiation in the 2θ range of 10°–80° at a scan rate of 8° min^{-1}. The morphologies and particle sizes of the materials were observed by scanning electron microscopy (SEM, JEOL JSM-6610 LV) and energy-dispersive spectroscopy (EDS, JEOL JSM-6610 LV). Transmission electron microscopy (TEM) and selected area electron diffraction (SAED) were carried out to further investigate the microstructure of materials by using a transmission electron microscope (JEOL JSM-2100F).

Electrochemical Measurement

The electrochemical performances of the prepared cathode materials were characterized by CR2032 coin-type half-cells. The working electrodes were made by mixing the cathode materials ($FeF_3{\cdot}0.33H_2O$ or $FeF_3{\cdot}0.33H_2O$/CNT), carbon black (Super P Li carbon), and polyvinylidene fluoride (PVDF) at a weight ratio of 90:5:5 in *N*-methyl pyrrolidinone (NMP). When the slurry was stirred uniform, it was pasted on an Al foil and dried at 85 °C overnight. The $FeF_3{\cdot}0.33H_2O$/C + G combination electrode was fabricated as mentioned above. The cathode electrodes were pressed and cut into several disks and weighted, and then they were dried at 85 °C for 4 h in a vacuum oven. The coin-type cells were assembled in an argon-filled glove box, where the oxygen and water contents were controlled to less than 0.1 ppm, metal Li foils as anodes and Celgard 2400 membrane as separator; 1.0 M $LiPF_6$ in ethylene carbonate (EC), propylene carbonate (PC), and diethyl carbonate (DEC) with a volume ratio of 1:1:1 were used as electrolyte. All the coin cells were aged for 4 h before testing. Galvanostatic charge/discharge tests were performed in the voltage range of 1.8–4.5 V (vs. Li^+/Li) on a Land battery test system (LAND CT-2001A, Wuhan, China) at room temperature. The specific capacities of the working electrodes were calculated based on the mass of the active cathode materials. Cyclic voltammetry (CV) and electrochemical impedance spectroscopy (EIS) were measured by an electrochemical workstation (CorrTest CS310). The scanning rate of the CV tests was 1 mV s^{-1} in the voltage range of 1.8–4.5 V (vs. Li^+/Li). The frequency range of EIS was from 100 kHz to 0.01 Hz at potentiostatic signal amplitudes of 5 mV.

Abbreviations

CNTs: Carbon nanotubes; CPE: Constant phase-angle element; CV: Cyclic voltammetry; DEC: Diethyl carbonate; D_{Li+}: Lithium ion diffusion coefficients; EC: Ethylene carbonate; EDS: Energy-dispersive spectroscopy;

EIS: Electrochemical impedance spectroscopy; EVs: Electric vehicles; $FeF_3{\cdot}0.33H_2O$/C + G: $FeF_3{\cdot}0.33H_2O$/CNT + graphene; HEVs: Hybrid electric vehicles; LIBs: Lithium-ion batteries; NMP: *N*-methyl pyrrolidinone; OMC: Ordered mesoporous carbon; PC: Propylene carbonate; PEDOT: poly (3,4-ethylenedioxythiophene); PEG: Polyethylene glycol; PVDF: Polyvinylidene fluoride; R_{ct}: Charge transfer resistance; R_s: Ohmic resistance; SAED: Selected area electron diffraction; SEM: Scanning electron microscopy; TEM: Transmission electron microscopy; TG-DSC: Thermogravimetric-differential scanning calorimetry; XRD: X-ray diffraction; Z_w: Warburg resistance

Funding
This work was supported by Science and Technology Plan Foundation of Guangdong (2017B010119002), Science and Technology Plan Foundation of Guangzhou (201803030015), and Science and Technology Plan Foundation of Guangzhou (201704030031).

Availability of Data and Materials
The data supporting the conclusions of this article are included within the article and its additional files.

Authors' Contributions
JL and LL designed the experiments. LL and SX performed the experiments. LL, SL, and LL analyzed the data. LL and SL wrote the manuscript. LL, YL, and SX drawn the figures. SH, CP, and FZ reviewed and edited the manuscript. All authors read and approved the final manuscript.

Ethics Approval and Consent to Participate
Not applicable.

Competing Interests
The authors declare that they have no competing interests.

Publisher's Note

Received: 18 October 2018 Accepted: 5 March 2019
Published online: 15 March 2019

References

1. Wang Y, Cao GZ (2008) Developments in nanostructured cathode materials for high-performance lithium-ion batteries. Adv Mater 20:2251–2269
2. Lee J, Kang B (2016) Novel and scalable solid-state synthesis of a nanocrystalline FeF_3/C composite and its excellent electrochemical performance. Chem Commun 52:9414–9417
3. Li JC, Zhang QL, Xiao XC, Cheng YT, Liang CD, Dudney NJ (2015) Unravelling the impact of reaction paths on mechanical degradation of intercalation cathodes for lithium-ion batteries. J Am Chem Soc 137:13732–13735
4. Xue L, Savilov SV, Lunin VV, Xia H (2018) Self-standing porous $LiCoO_2$ nanosheet arrays as 3D cathodes for flexible li-ion batteries. Adv Funct Mater 28:1705836
5. Lai FY, Zhang XH, Wu Q, Zhang JJ, Li QY, Huang YG, Liao Z, Wang HQ (2018) Effect of surface modification with spinel $NiFe_2O_4$ on enhanced cyclic stability of $LiMn_2O_4$ cathode material in lithium ion batteries. ACS Sustain Chem Eng 6:570–578
6. Chen MF, Wang XY, Shu HB, Yu RZ, Yang XK, Huang WH (2015) Solvothermal synthesis of monodisperse micro-nanostructure starfish-like porous $LiFePO_4$ as cathode material for lithium-ion batteries. J Alloys Compd 652:213–219
7. Wang F, Kim SW, Seo DH, Kang K, Wang LP, Su D, Vajo JJ, Wang J, Graetz J (2015) Ternary metal fluorides as high-energy cathodes with low cycling hysteresis. Nat Commun 6:6668
8. Li CL, Mu XK, Aken PAV, Maier J (2013) A high-capacity cathode for lithium batteries consisting of porous microspheres of highly amorphized iron fluoride densified from its open parent phase. Adv Energy Mater 3:113–119
9. Li LS, Jacobs R, Gao P, Gan LY, Wang F, Morgan D, Jin S (2016) Origins of large voltage hysteresis in high-energy-density metal fluoride lithium-ion battery conversion electrodes. J Am Chem Soc 138:2838–2848
10. Rao RS, Pralong V, Varadaraju UV (2016) Facile synthesis and reversible lithium insertion studies on hydrated iron trifluoride $FeF_3{\cdot}0.33H_2O$. Solid State Sci 55:77–82
11. Li Y, Zhou XZ, Bai Y, Chen GH, Wang ZH, Li H, Wu F, Wu C (2017) Building an electronic bridge via Ag decoration to enhance kinetics of iron fluoride cathode in lithium-ion batteries. ACS Appl Mater Interfaces 9:19852–19860
12. Tan JL, Liu L, Hu H, Yang ZH, Guo HP, Wei QL, Yi X, Yan ZC, Zhou Q, Huang ZF, Shu HB, Yang XK, Wang XY (2014) Iron fluoride with excellent cycle performance synthesized by solvothermal method as cathodes for lithium ion batteries. J Power Sources 251:75–84
13. Zhou MJ, Zhao LW, Okada S, Yamaki JI (2014) Quantitative studies on thermal stability of a FeF_3 cathode in methyl difluoroacetate-based electrolyte for Li-ion batteries. J Power Sources 253:74–79
14. Ali G, Rahman G, Chung KY (2017) Cobalt-doped pyrochlore-structured iron fluoride as a highly stable cathode material for lithium-ion batteries. Electrochim Acta 238:49–55
15. Liu M, Wang XY, Wei SY, Hu H, Zhang R, Liu L (2018) Cr-doped $Fe_2F_5 \quad H_2O$ with open framework structure as a high performance cathode material of sodium-ion batteries. Electrochim Acta 269:479–489
16. Liu M, Wang XY, Zhang R, Liu L, Hu H, Wang Y, Wei SY (2018) Hollow porous $FeF_3{\cdot}0.33H_2O$ microspheres by $AlPO_4$ coating as a cathode material of Na-ion batteries. J Energy Storage 18:103–111
17. Ma DL, Cao ZY, Wang HG, Huang XL, Wang LM, Zhang XB (2012) Three-dimensionally ordered macroporous FeF_3 and its in situ homogenous polymerization coating for high energy and power density lithium ion batteries. Energy Environ Sci 5:8538
18. Li LP, Zhu JH, Xu MW, Jiang J, Li CM (2017) In situ engineering toward core regions: a smart way to make applicable FeF_3@carbon nanoreactor cathodes for Li-ion batteries. ACS Appl Mater Interfaces 9:17992–18000
19. Yang J, Xu ZL, Sun HX, Zhou XY (2016) A three-dimensional interlayer composed of graphene and porous carbon for long-life, high capacity lithium-iron fluoride battery. Electrochim Acta 220:75–82
20. Wu W, Wang Y, Wang XY, Chen QQ, Wang X, Yang SY, Liu XM, Guo J, Yang ZH (2009) Structure and electrochemical performance of FeF_3/V_2O_5 composite cathode material for lithium-ion battery. J Alloys Compd 486:93–96
21. Zhou XY, Sun HX, Zhou HC, Ding J, Xu ZL, Bin WJ, Tang JJ, Yang J (2018) Enhancing the lithium storage capacity of FeF_3 cathode material by introducing C@LiF additive. J Electroanal Chem 810:41–47
22. Jung H, Shin J, Chae C, Lee JK, Kim J (2013) FeF_3/ordered mesoporous carbon (OMC) nanocomposites for lithium ion batteries with enhanced electrochemical performance. J Phys Chem C 117:14939–14946
23. Li BJ, Cheng ZJ, Zhang NQ, Sun KN (2014) Self-supported, binder-free 3D hierarchical iron fluoride flower-like array as high power cathode material for lithium batteries. Nano Energy 4:7–13
24. Ali G, Lee JH, Cho BW, Nam KW, Ahn D, Chang W, Oh SH, Chung KY (2016) Probing the sodiation-desodiation reactions in nano-sized iron fluoride cathode. Electrochim Acta 191:307–316
25. Shen YQ, Wang XY, Hu H, Jiang ML, Yang XK, Shu HB (2015) A graphene loading heterogeneous hydrated forms iron based fluoride nanocomposite as novel and high-capacity cathode material for lithium/sodium ion batteries. J Power Sources 283:204–210
26. Pohl A, Faraz M, Schröder A, Baunach M, Schabel W, Guda A, Shapovalov V, Soldatov A, Chakravadhanula VSK, Kübel C, Witte R, Hahn H, Diemant T, Behm RJ, Emerich H, Fichtner M (2016) Development of a water based process for stable conversion cathodes on the basis of FeF_3. J Power Sources 313:213–222
27. Liu L, Guo HP, Zhou M, Wei QL, Yang ZH, Shu HB, Yang XK, Tan JL, Yan ZC, Wang XY (2013) A comparison among $FeF_3 \quad 3H_2O$, $FeF_3 \quad 0.33H_2O$ and FeF_3 cathode materials for lithium ion batteries: structural, electrochemical, and mechanism studies. J Power Sources 238:501–515
28. Huang C, Ouyang T, Zou Y, Li N, Liu ZQ (2018) Ultrathin $NiCo_2P_x$ nanosheets strongly coupled with CNTs as efficient and robust electrocatalysts for overall water splitting. J Mater Chem A 6:7420–7427
29. Kim BSW, Seo DH, Gwon H, Kim J, Kang K (2010) Fabrication of FeF_3 nanoflowers on CNT branches and their application to high power lithium rechargeable batteries. Adv Mater 22:5260–5264
30. Li BJ, Rooney DW, Zhang NQ, Sun KN (2013) An in situ ionic-liquid-assisted synthetic approach to Iron fluoride/graphene hybrid nanostructures as superior cathode materials for lithium ion batteries. ACS Appl Mater Interfaces 5:5057–5063

31. Liu J, Wan YL, Liu W, Ma ZS, Ji SM, Wang JB, Zhou YC, Hodgson P, Li YC (2013) Mild and cost-effective synthesis of iron fluoride–graphene nanocomposites for high-rate Li-ion battery cathodes. J Mater Chem A 1:1969
32. Hu XB, Ma MH, Mendes RG, Zeng MQ, Zhang Q, Xue YH, Zhang T, Rummeli MH, Fu L (2015) Li-storage performance of binder-free and flexible iron fluoride@graphene cathodes. J Mater Chem A 3:23930–23935
33. Bao TT, Zhong H, Zheng HY, Zhan H, Zhou YH (2015) In-situ synthesis of FeF_3/graphene composite for high-rate lithium secondary batteries. Electrochim Acta 176:215–221
34. Cheng H, Li ML, Su CY, Li N, Liu ZQ (2017) Cu-co bimetallic oxide quantum dot decorated nitrogen-doped carbon nanotubes: a high-efficiency bifunctional oxygen electrode for Zn–air batteries. Adv Funct Mater 27:1701833
35. Chen X, Oh WD, Lim TT (2018) Graphene-and CNTs-based carbocatalysts in persulfates activation: material design and catalytic mechanisms. Chem Eng J 354:941–976
36. Li CL, Gu L, Tong JW, Maier J (2011) Carbon nanotube wiring of electrodes for high-rate lithium batteries using an imidazolium-based ionic liquid precursor as dispersant and binder: a case study on Iron fluoride nanoparticles. ACS Nano 5:2930–2938
37. Ji HX, Zhang LL, Pettes MT, Li HF, Chen SS, Shi L, Piner R, Ruoff RS (2012) Ultrathin graphite foam: a three-dimensional conductive network for battery electrodes. Nano Lett 12:2446–2451
38. Wang HL, Yang Y, Liang YY, Robinson JT, Li YG, Jackson A, Cui Y, Dai HJ (2011) Graphene-wrapped sulfur particles as a rechargeable lithium-sulfur battery cathode material with high capacity and cycling stability. Nano Lett 11:2644–2647
39. Xiao J, Wang XJ, Yang XQ, Xun SD, Liu G, Koech PK, Liu J, Lemmon JP (2011) Electrochemically induced high capacity displacement reaction of PEO/MoS_2/graphene nanocomposites with lithium. Adv Funct Mater 21:2840–2846
40. Chou SL, Wang JZ, Choucair M, Liu HK, Stride JA, Dou SX (2010) Enhanced reversible lithium storage in a nanosize silicon/graphene composite. Electrochem Commun 12:303–306
41. Luo D, Li GS, Fu CC, Zheng J, Fan JM, Li Q, Li LP (2014) A new spinel-layered Li-rich microsphere as a high-rate cathode material for Li-ion batteries. Adv Energy Mater 4:1400062